J. Fluid Mech. (2025), *vol.* 1016, A58, doi:10.1017/jfm.2025.10412

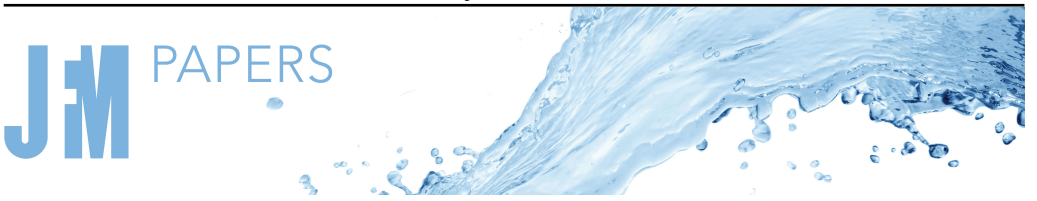

Turbulent skin-friction drag reduction via spanwise forcing at high Reynolds number

Davide Gatti[1], **Maurizio Quadrio**[2], **Alessandro Chiarini**[2,3], **Federica Gattere**[2] and **Sergio Pirozzoli**[4]

[1]Institute of Fluid Mechanics, Karlsruhe Institute of Technology, Kaiserstraße 10, 76131 Karlsruhe, Germany

[2]Dipartimento di Scienze e Tecnologie Aerospaziali, Politecnico di Milano, via La Masa 34, 20156 Milano, Italy

[3]Complex Fluids and Flows Unit, Okinawa Institute of Science and Technology Graduate University, 1919-1, Tancha, Onna-son, Okinawa 904-0495, Japan

[4]Dipartimento di Meccanica e Aeronautica, Università di Roma 'La Sapienza', via Eudossiana 18, 00184 Rome, Italy

Corresponding author: Davide Gatti, davide.gatti@kit.edu

(Received 19 August 2024; revised 26 May 2025; accepted 31 May 2025)

We address the Reynolds number dependence of the turbulent skin-friction drag reduction induced by streamwise-travelling waves of spanwise wall oscillations. The study relies on direct numerical simulations of drag-reduced flows in a plane open channel at friction Reynolds numbers in the range $1000 \leqslant Re_\tau \leqslant 6000$, which is the widest range considered so far in simulations with spanwise forcing. Our results corroborate the validity of the predictive model proposed by Gatti & Quadrio (*J. Fluid Mech.* vol. 802, 2016, pp. 553–558): regardless of the control parameters, the drag reduction decreases monotonically with Re at a rate that depends on the drag reduction itself and on the skin-friction of the uncontrolled flow. We do not find evidence in support of the results of Marusic *et al.* (*Nat. Commun.* vol. 12, no. 1, 2021, pp. 5805), which instead report by experiments an increase of the drag reduction with Re in turbulent boundary layers, for control parameters that target low-frequency, outer-scaled motions. Possible explanations for this discrepancy are provided, including obvious differences between open channel flows and boundary layers, and possible limitations of laboratory experiments.

Key words: drag reduction, flow control, turbulence control

1. Introduction

Transverse near-wall forcing as a means to mitigate skin-friction drag in turbulent flows has garnered significant attention, owing to its potential for substantial environmental and economic benefits (Quadrio 2011; Ricco, Skote & Leschziner 2021). After the seminal work on spanwise wall oscillations by Jung, Mangiavacchi & Akhavan (1992), three decades of research efforts have led to important progress; however, several crucial factors still hinder the deployment of spanwise forcing in technological settings. While devising viable and efficient implementations of the typically idealised near-wall forcing is the major challenge, additional concerns exist, including the decreasing effectiveness of drag reduction with increasing Reynolds numbers (Re).

To date, the Reynolds number dependence of skin-friction drag reduction has mostly been studied in the context of streamwise-travelling waves of spanwise wall velocity (StTW, Quadrio, Ricco & Viotti 2009), a specific form of transverse forcing characterised by its comparatively large potential for drag reduction with moderate energy expenditure. StTW are described by

$$w_w(x, t) = A \sin(\kappa x - \omega t), \tag{1.1}$$

where w_w is the spanwise (z) velocity component at the wall, A is the maximum wall velocity and thus a measure of the amplitude of the spanwise forcing, κ is the streamwise wavenumber, ω is the angular frequency, and x and t are the streamwise coordinate and the time. The forcing, sketched in figure 1, consists of streamwise-modulated waves of spanwise velocity at the wall, with wavelength $\lambda = 2\pi/\kappa$ and period $T = 2\pi/\omega$. The waves travel along the streamwise direction with phase speed $c = \omega/\kappa$, either downstream ($c > 0$) or upstream ($c < 0$) with respect to the mean-flow direction. The forcing described by (1.1) includes the two special cases of spatially uniform spanwise wall oscillations (Quadrio & Ricco 2004) for $\kappa = 0$ and steady waves (Viotti, Quadrio & Luchini 2009) for $\omega = 0$. With the appropriate set of control parameters, StTW have been shown to yield considerable drag reduction in a series of numerical experiments regarding channel and pipe flows (Quadrio *et al.* 2009; Gatti & Quadrio 2013; Hurst, Yang & Chung 2014; Gatti & Quadrio 2016; Liu *et al.* 2022; Rouhi *et al.* 2023; Gallorini & Quadrio 2024) and boundary layers (Skote *et al.* 2015; Skote 2022), as well as in laboratory experiments (Auteri *et al.* 2010; Bird, Santer & Morrison 2018; Chandran *et al.* 2023). In addition to canonical flows, including the compressible and supersonic regimes (Gattere *et al.* 2024), StTW have been applied to more complex flows ranging from channels with curved walls (Banchetti, Luchini & Quadrio 2020) to rough boundary layers (Deshpande, Kidanemariam & Marusic 2024) (although restricted to spatially uniform spanwise wall oscillation) and transonic aerofoils with shock waves (Quadrio *et al.* 2022), showing that local skin-friction drag reduction can be exploited to also reduce the pressure component of the aerodynamic drag.

Understanding how the Reynolds number affects drag reduction by StTW is a particularly challenging goal for three main reasons. First, a sufficiently wide portion of a huge parameter space must be explored, which, even in simple canonical flows, includes the four parameters $\{A, \kappa, \omega; Re\}$, and poses a great challenge to numerical and laboratory experiments.

A second complication is the choice of an appropriate figure of merit for drag reduction. Typically, the drag reduction rate $\mathcal{R}$ is defined as

$$\mathcal{R} = 1 - \frac{C_f}{C_{f_0}}, \tag{1.2}$$

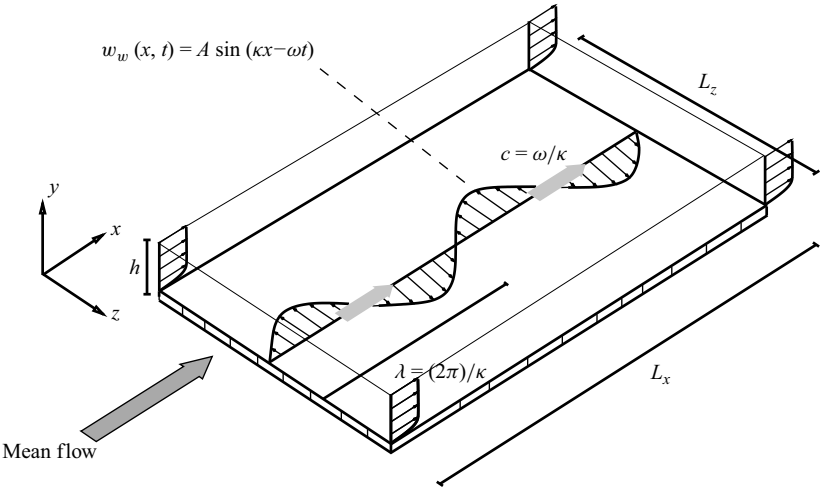

Figure 1. Schematic of a turbulent open channel flow actuated with streamwise-travelling waves of spanwise wall velocity with amplitude A, streamwise wavenumber κ and angular frequency ω. Here, λ is the streamwise wavelength; c is the wave phase speed; and L_x, $L_y = h$ and L_z are the dimensions of the computational domain in the streamwise, wall-normal and spanwise direction, respectively.

i.e. as the control-induced relative change of the skin-friction coefficient C_f (Kasagi *et al.* 2009). In (1.2) and in the remainder of this manuscript, the subscript '0' denotes quantities measured in the reference uncontrolled flow. Specifically, C_f is defined as $C_f = 2\tau_x/(\rho U_b^2)$; τ_x is the mean streamwise wall shear stress, U_b the bulk velocity and ρ the fluid density. However, as observed by Gatti & Quadrio (2016), the quantity $\mathcal{R}$ defined by (1.2) is inherently Re-dependent, owing to the Re dependence of C_f and C_{f_0}. This is long known to be the case for the flow over rough surfaces (Nikuradse 1933; Jiménez 2004), as well as for other flow control techniques relying on near-wall turbulence manipulation such as riblets (Luchini 1996; Spalart & McLean 2011). Choosing a figure of merit which eliminates this trivial dependency on the Reynolds number is crucial to describe properly the Re effect on drag reduction.

Third, the wall-shear stress generally differs in the reference (τ_{x_0}) and controlled (τ_x) channel flows, unless they are driven by the same pressure gradient (as done for example by Ricco *et al.* 2012); hence, the viscous scaling becomes ambiguous. As noted by Quadrio (2011), this results in two possible viscous normalisations of the controlled flow: the first, denoted with the superscript '+', relies on the reference friction velocity $u_{\tau_0} = \sqrt{\tau_{x_0}/\rho}$; the second, denoted with the superscript '$*$', is based on the actual friction velocity $u_\tau = \sqrt{\tau_x/\rho}$. Similarly, two different friction Reynolds numbers, $Re_{\tau_0} = u_{\tau_0}h/\nu$ and $Re_\tau = u_\tau h/\nu$, can be defined depending on the choice of the friction velocity. Here, h describes the half-height of a channel or the depth of an open channel, and ν is the fluid kinematic viscosity. While the actual viscous scaling is the only sensible choice for the drag-reduced flow (Gatti & Quadrio 2016), the reference scaling is necessary when the wall friction of the drag-reduced flow is not known yet.

Gatti & Quadrio (2016), indicated also as GQ16 hereinafter, circumvented these difficulties by designing a campaign of several thousands of direct numerical simulation (DNS) runs of turbulent channel flows. Inspired by similar studies on rough walls (see for example Leonardi *et al.* 2015), they limited the otherwise prohibitive computational cost by choosing relatively small computational domains (Jiménez & Moin 1991; Flores & Jiménez 2010) for most of the study. At the expense of a residual domain-size dependence

of the results, which cancels out in large part when observing the difference between controlled and uncontrolled flows, GQ16 generated a large dataset, along with a more limited number of simulations in wider domains to verify the accuracy of the results. This approach enabled not only the inspection of a large portion of the $\{A, \kappa, \omega\}$-space at $Re_{\tau_0} = 200$ and 1000, but also the transfer of the dataset between viscous '+' and '$*$' units via interpolation, allowing to assess the results in both scalings. Thanks to their comprehensive database (available as Supplementary Material to their paper), Gatti & Quadrio (2016) challenged the then-current belief that skin-friction drag reduction was bound to decrease quickly with Re. They demonstrated that the drag reduction effect by spanwise forcing becomes in fact constant with Re, provided that it is not expressed via $\mathcal{R}$ (1.2), that is *per se* Re-dependent, but through the Reynolds number invariant parameter ΔB^*. The quantity ΔB^* expresses the main effect of the StTW, which is to induce a change of the additive constant in the logarithmic law for the mean velocity profile

$$U^*(y^*) = \frac{1}{k} \ln y^* + B_0^* + \Delta B^* , \tag{1.3}$$

where k is the von Kármán constant, B_0^* is the additive constant in the reference channel flow and $B^* = B_0^* + \Delta B^*$ is the additive constant of the controlled flow. The independence of ΔB^* upon Re is a common feature of all turbulence manipulations whose action is confined to the near-wall region. In these cases, the outer turbulence simply reacts to a wall layer with different drag (Gatti *et al.* 2018), as well known, for instance, in the context of drag-reducing riblets (Luchini 1996; Garcia-Mayoral & Jiménez 2011; Spalart & McLean 2011) and drag-increasing roughness (Clauser 1954; Hama 1954).

Under the assumption that ΔB^* is a function of the control parameters $\{A^*, \kappa^*, \omega^*\}$, but not of the Reynolds number, Gatti & Quadrio (2016) derived the following modified friction relation (hereinafter called GQ model):

$$\Delta B^* = \sqrt{\frac{2}{C_{f_0}}} \left[(1 - \mathcal{R})^{-1/2} - 1 \right] - \frac{1}{2k} \ln (1 - \mathcal{R}) , \tag{1.4}$$

where the Re dependence is not explicit, but rather embedded in C_{f_0}. Provided the function $\Delta B^*(A^*, \kappa^*, \omega^*)$ is measured at a sufficiently large Re for the log law in (1.3) to hold, the GQ model predicts $\mathcal{R}$ at any arbitrary value of Re. According to (1.4), $\mathcal{R}$ is always expected to decrease with Re for any combination of the control parameters, but at much lower rate than suggested by previous studies (Touber & Leschziner 2012; Gatti & Quadrio 2013; Hurst *et al.* 2014), so that significant drag reduction can be still achieved at Reynolds numbers typical of technological applications. For instance, for StTW, GQ16 estimated possible drag reduction of 30 % with $A^+ = 12$ at $Re_{\tau_0} = 10^5$.

The GQ16 study is affected by two limitations. First, $Re_{\tau_0} = 1000$, the largest Re considered in their study, may still be not enough for ΔB^* to become completely Re-independent: GQ16 suggested that at least $Re_{\tau_0} = 2000$ should be considered. Second, the small residual effect of the restricted computational box sizes on the quantification of $\mathcal{R}$ could, in principle, bias the extrapolation to higher Re. Nonetheless, the GQ model passed validation tests against previous (Touber & Leschziner 2012; Hurst *et al.* 2014) and later literature data. For instance, Rouhi *et al.* (2023) employed large eddy simulation (LES) to study drag reduction by StTW in open channel flows at $Re_{\tau_0} = 945$ and $Re_{\tau_0} = 4000$. They explored the parameter space within the range $\kappa^+ \in [0.002, 0.02]$ and $\omega^+ \in [-0.2, 0.2]$, at fixed $A^+ = 12$. This is to be compared with $\kappa^+ \in [0, 0.05]$ and $\omega^+ \in [-0.5, 1]$ addressed by Gatti & Quadrio (2016), who also considered various amplitudes $A^+ \in [2, 20]$. The study of Rouhi *et al.* (2023) is however limited by the use of LES, in which part of the

small-scale turbulence physics involved in drag reduction is modelled, and by the domain size ($L_x = 2.04h$, $L_z = 0.63h$ at $Re_{\tau_0} = 4000$), which is comparable to the restricted domain size ($L_x = 1.35h$, $L_z = 0.69h$ at $Re_{\tau_0} = 1000$) considered by Gatti & Quadrio (2016), despite the larger Re_{τ_0}. Rouhi *et al.* (2023) confirmed that the GQ model predicts very well their drag reduction data, with deviations of the order of 2 %, for all StTW control parameters sufficiently far from those yielding drag increase.

Marusic *et al.* (2021) and Chandran *et al.* (2023) studied drag reduction via backward-travelling ($c < 0$) StTW. Their experimental study was carried out in a zero pressure gradient turbulent boundary layer up to the largest values of Re investigated so far, $Re_\tau = 15\,000$. By extending to the plane geometry the actuation strategy used by Auteri *et al.* (2010) in a cylindrical pipe, they implemented the ideal forcing of (1.1) by dividing a portion of the wall into a series of forty-eight slats, each 5 cm long, so that each six consecutive slats constitute a single wavelength with fixed $\lambda = 0.3$ m. The slats move in the spanwise direction at a fixed half-stroke d, resulting in a frequency-dependent maximum spanwise velocity $A = \omega d$. As a consequence, in those experiments, the amplitude and period of the oscillations could not be varied independently. With d and λ constant in physical units, the range of investigated parameters shifts towards smaller κ^+, ω^+ and A^+ as Re_{τ_0} increases. The authors observed, for the first time, $\mathcal{R}$ to increase with Re (see figure 3(e) of Marusic *et al.* 2021), and explained it by the particularly slow time scale $T^+ = 2\pi/\omega^+ < -350$ of their forcing, which was meant to target the large inertial, outer-scaled structures of turbulence (Deshpande *et al.* 2023), whose importance increases with Re.

Despite the promising results, these studies also have shortcomings. With d and λ constant in physical units, which is unavoidable in laboratory experiments, the control parameters could not be kept constant in either '+' or '$*$' viscous units while varying Re_{τ_0}. In particular, the fixed wavelength leads to a κ^+ that decreases with Re. Furthermore, the effect of ω and A cannot be addressed separately. This precludes the investigation of the full space of the control parameters: for instance, large values of ω^+ at low A^+ cannot be tested. Lastly, the key observation that $\mathcal{R}$ increases with Re relies on the joint observation of low-Re LES data by Rouhi *et al.* (2023) obtained in an open channel flow and high-Re experimental data by Marusic *et al.* (2021) in a boundary layer, thus bringing together different methods and flow configurations.

The present research fills these gaps in the existing literature by leveraging a novel DNS dataset of turbulent open channel flow to accurately quantify the Reynolds number effects on the drag-reducing performance of StTW. The computational domain adopted in the present simulations is large enough to properly account for all relevant scales of turbulence, including the large inertial scales. The considered Reynolds numbers, ranging from $Re_{\tau_0} = 1000$ to $Re_{\tau_0} = 6000$, are large enough to minimise the low-Re effects, matching some of the experimental data points by Chandran *et al.* (2023). The dataset is further designed to address the Reynolds number scaling of drag reduction in both viscous and outer units independently, by considering the same flow configuration and by using the same numerical method for all Re.

The paper is organised as follows. After this Introduction, § 2 describes the computational procedure and the simulation parameters used to produce the DNS dataset. In § 3, the effect of the Reynolds number is analysed in terms of both drag reduction and power budgets, and compared with existing literature. Finally, concluding arguments are given in § 4.

2. Methods and procedures

A new DNS dataset of incompressible turbulent open-channel flows (see figure 1) is used to study the effect of the Reynolds number on the reduction of the turbulent friction

Re_b	Re_{τ_0}	N_{cases}	L_x/h	L_z/h	$N_x \times N_y \times N_z$	Symbol
20 000	996.7	71	$6\pi h$	$2\pi h$	$2304 \times 165 \times 1536$	▲
43 650	1994.1	62	$6\pi h$	$2\pi h$	$4608 \times 265 \times 3072$	▼
68 600	3008.8	7	$6\pi h$	$2\pi h$	$6912 \times 355 \times 4608$	♦
148 000	6012.6	2	$6\pi h$	$2\pi h$	$13312 \times 591 \times 9216$	●

Table 1. Details of the direct numerical simulations of open channel flows (including domain size and discretisation) modified by StTW, grouped in sets of N_{cases} simulations performed at a constant value of bulk Reynolds number $Re_b = U_b h/\nu$. The last column indicates the colour and symbol employed in the following figures to represent each set of simulations.

drag achieved by StTW. The open channel flow, i.e. half a channel flow with a symmetry boundary condition at the centreplane, is considered here to reduce the computational cost without affecting the drag reduction results; indeed, it was often used in the past, including e.g. the similar studies by Yao, Chen & Hussain (2022), Pirozzoli (2023) and Rouhi *et al.* (2023). The StTW are applied as a wall boundary condition for the spanwise velocity component after (1.1). Periodic boundary conditions are applied in the homogeneous streamwise and spanwise directions, no-slip and no-penetration boundary conditions are used for the longitudinal and wall-normal components at the bottom wall; free slip is used at the top boundary. The computational set-up is identical to that in the study of Pirozzoli (2023), in which open-channel flow was studied in the absence of flow control. The solver relies on the classical fractional step method with second-order finite differences on a staggered grid (Orlandi 2006). The Poisson equation resulting from the divergence-free condition is efficiently solved via Fourier expansion in the periodic directions (Kim & Moin 1985). The governing equations are advanced in time starting from the initial condition of a statistically stationary, uncontrolled turbulent open channel flow by means of a hybrid third-order, low-storage Runge–Kutta algorithm, whereby the diffusive terms are handled implicitly. Statistical averaging, indicated hereinafter as $\langle\cdot\rangle$, implies averaging in time and along the two homogeneous directions.

Four sets of simulations, whose details are listed in table 1, are run at prescribed values of the bulk Reynolds number $Re_b = U_b h/\nu$; the bulk velocity is kept constant at every time step as described by Quadrio, Frohnapfel & Hasegawa (2016). Each set comprises one reference simulation, in which the wall is steady, and a variable number of cases with StTW at different values of $\{A, \kappa, \omega\}$. In the following, we will refer to each simulation set via its (nominal) value of Re_{τ_0}; the actual values of Re_τ vary throughout simulations of each set, as a consequence of the wall actuation at constant U_b.

All DNS investigations are carried out in a domain with $L_x = 6\pi h$ and $L_z = 2\pi h$, which is much larger than what has been adopted by Rouhi *et al.* (2023) and GQ16 at similar values of Re, but a bit smaller than the domain used by Yao *et al.* (2022). Whereas weak longitudinal eddies may be not resolved, a box sensitivity study carried out by Pirozzoli (2023) showed that the practical impact on the leading-order flow statistics and on the spanwise spectra is extremely small.

Figure 2 indeed supports the adequacy of the present computational box by analysing the streamwise velocity fluctuations of the reference open channel flow at $Re_{\tau_0} = 6000$, i.e. the largest Reynolds number considered in the present study. Figure 2(*a*) shows the spanwise pre-multiplied spectrum $k_z^+ \phi_{uu}^+$, where k_z is the spanwise wavenumber and ϕ_{uu} is a component of the velocity spectrum tensor, with a clear outer peak visible at $\lambda_z \approx h$. Figure 2(*b*) shows the variance $\langle uu \rangle^+$ of the streamwise velocity, split into the large-scale $\langle uu \rangle_L^+$ and small-scale $\langle uu \rangle_S^+$ contributions. The large-scale contribution is obtained by

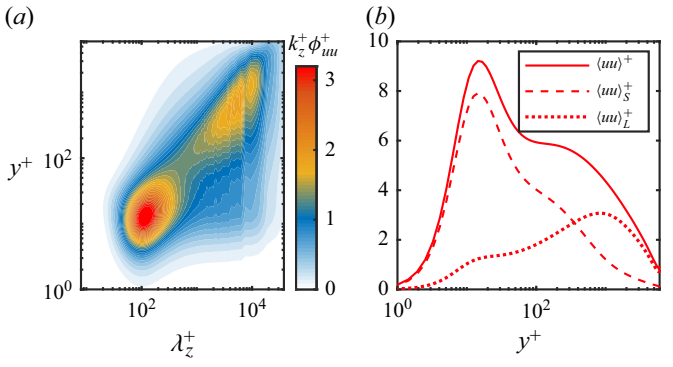

Figure 2. Statistics of streamwise velocity fluctuations for the reference simulation at $Re_{\tau_0} = 6000$: (*a*) spanwise premultiplied spectra $k_z^+\phi_{uu}^+$; (*b*) streamwise variance $\langle uu\rangle^+$ with its large-scale $\langle uu\rangle_L^+$ and small-scale $\langle uu\rangle_S^+$ contributions. Large scales are defined as those for which $2\pi/k_z > 0.5h$.

integrating the spectrum only for wavelengths $\lambda_z > 0.5h$ as suggested by Bernardini & Pirozzoli (2011), Dogan *et al.* (2019) and Yao *et al.* (2022). With this definition, the large-scale fluctuations are responsible for 12 % of the total variance in the vicinity of the wall, and for as much as 85 % at the free-slip surface. Moreover, it should be noted that the longest travelling wave that we have tested at the highest Reynolds number ($Re_{\tau_0} = 6000$) is fourteen times shorter than the domain length, thus allowing subharmonic effects, if present, to be properly resolved.

The spatial resolution of the simulations is designed based on the criteria discussed by Pirozzoli & Orlandi (2021). In particular, the collocation points are distributed in the wall-normal direction y so that approximately thirty points are placed within $y^+ \leqslant 40$, with the first grid point at $y^+ < 0.1$. The mesh is stretched in the outer wall layer with the mesh spacing proportional to the local Kolmogorov length scale, which there varies as $\eta^+ \approx 0.8(y^+)^{1/4}$ (Jiménez 2018). A mild refinement towards the free surface is used to resolve the thin layer in which the top boundary condition dampens the wall-normal velocity fluctuations. The grid resolution in the wall-parallel directions is set to $\Delta x^+ \approx 8.5$ and $\Delta z^+ \approx 4.0$ for all the flow cases. Note that the resolution becomes finer in actual viscous units in all cases with drag reduction.

Figure 3 shows at a glance the range of the StTW parameters addressed in the present study for the simulation sets at $Re_{\tau_0} = \{1000, 2000, 3000, 6000\}$. This is the widest range of Re considered so far in numerical simulations with spanwise wall forcing.

The portion of the $\{\kappa^+, \omega^+\}$-space spanned in the present study is smaller than that addressed in GQ16. In fact, we limit ourselves to considering $\kappa^+ \leqslant 0.02$ and $|\omega^+| \leqslant 0.1$, which is now known to be the most interesting part of the parameter space, where the maxima of drag reduction $\mathcal{R}$ and net saving $\mathcal{S}$ are expected.

The control parameters have been selected according to the following guiding principles.

(i) The intent to further scrutinise the validity of the results by GQ16, obtained in constrained computational domains, led us to consider a wider portion of the StTW parameter space at $Re_{\tau_0} = 1000$, the highest value considered in their study.
(ii) GQ16 observed that ΔB^* may still retain residual dependence on Re at their highest value of $Re_{\tau_0} = 1000$ and suggested that at least $Re_{\tau_0} = 2000$ is needed for an Re-independent measure. Therefore, the same region of the parameter space considered in point (i) is also considered at $Re_{\tau_0} = 2000$.

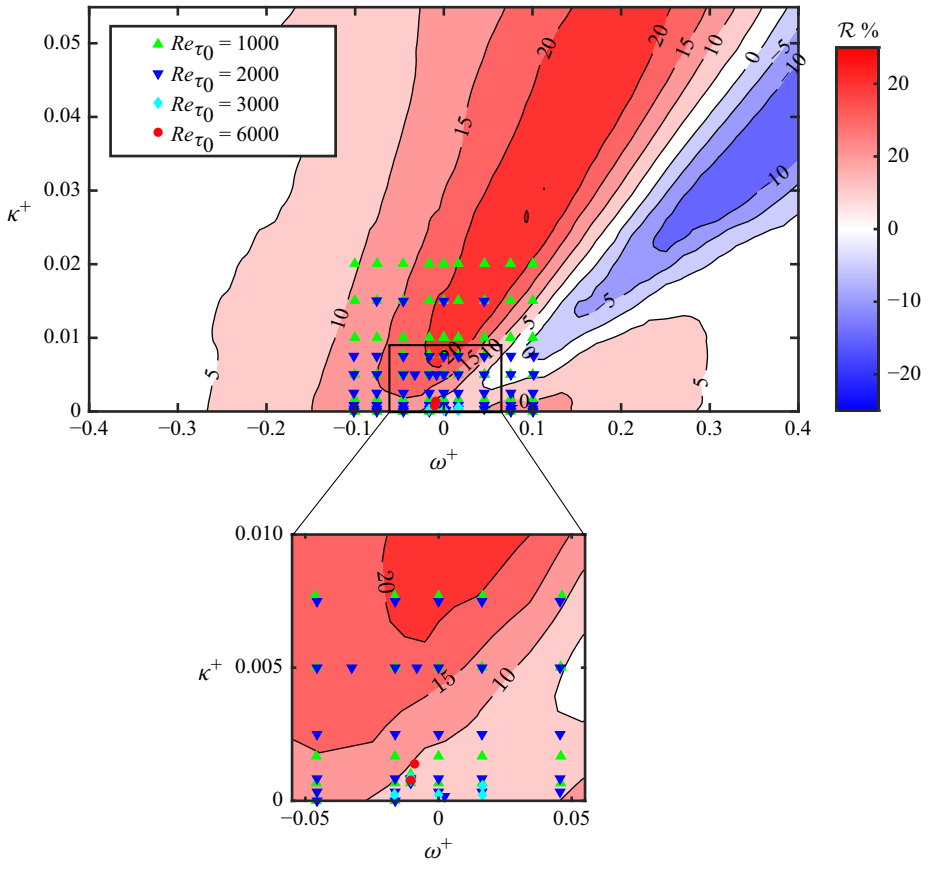

Figure 3. Portion of the parameter space spanned in the present study overlaid to the drag reduction map by GQ16 computed at $A^+ = 5$. Each symbol corresponds to one simulation at the Reynolds number encoded by its shape/colour, as described by the legend.

(iii) Marusic *et al.* (2021) reported for the first time a drag reduction that increases with Re for small values of κ^+ and ω^+, in particular for $\kappa^+ = 0.0008$ (i.e. $\lambda^+ \approx 8000$), $\omega^+ = -0.0105$ (i.e. $T^+ \approx -600$) and $A^+ \approx 5$ (in fact, their A^+ varies slightly across the Rerange), as shown in figure 3(*e*) of their paper. We have added this combination of $\{\kappa^+, \omega^+\}$ to all simulations sets to verify the increase of $\mathcal{R}$ with Re. This is one of the two controlled cases we have carried out at $Re_{\tau_0} = 6000$. The second case, with $\kappa^+ = 0.0014$, $\omega^+ = -0.009$ and $A^+ = 2.5$, matches exactly one of the cases considered experimentally by Chandran *et al.* (2023), at the same value of $Re_{\tau_0} = 6000$.

(iv) All controlled simulations are performed at $A^+ = 5$ for two reasons: first, this value of A^+ is representative of the amplitude range in the experiments by Marusic *et al.* (2021) for the case discussed in point (iii); second, this value is close to $A^+ \approx 6$ at which GQ16 measured the maximum of net power saving $\mathcal{S}$. By adopting this value of A^+, we can verify whether positive $\mathcal{S}$ can also be achieved at higher Re.

This results in the set of control parameters shown in figure 3, and listed in tables 2, 3, 4 and 5 of Appendix A together with the main results. As will be clarified in the following, understanding the Re dependence of $\mathcal{R}$ and $\mathcal{S}$ requires accurate estimation of

the mean wall friction, which we guarantee by monitoring statistical uncertainty via the method described by Russo & Luchini (2017), as shown in figures 6 and 9. Statistics are accumulated for at least $10h/u_{\tau_0}$ time units after the initial transient, during which the control leads the flow towards a reduced level of drag.

3. Results

The outcomes of the present study are presented following the guiding principles outlined in § 2. First, we present drag reduction maps at $Re_{\tau_0} = 1000$ and 2000, and use them to provide ultimate validation of the GQ16 results. Second, we evaluate ΔB^* at $Re_{\tau_0} = 2000$ and verify the Re independence of this drag reduction metric. Third, drag reduction is reported up to $Re_{\tau_0} = 6000$ for the same actuation parameters for which Marusic *et al.* (2021) observed drag reduction increase with Re. Finally, the possibility to achieve net power savings at high Re is discussed.

3.1. *Maps of $\mathcal{R}$: validity of the results by GQ16*

Figure 4 compares the present drag reduction results at $Re_{\tau_0} = 1000$ and $Re_{\tau_0} = 2000$ with the data by GQ16, which need to be transferred to the present values of Re_{τ_0}. The procedure involves starting from their $\mathcal{R}$ and C_{f_0} data, then using the GQ model ((1.4) with $k = 0.39$; GQ16 showed that the specific value of k in the range 0.385–0.4 does not significantly affect the results) to compute ΔB^*. The resulting cloud of ΔB^* data points at discrete $\{A^+, \kappa^+, \omega^+\}$ values is linearly interpolated on a Cartesian grid spanning the $\{\kappa^+, \omega^+\}$ space at the value of $A^+ = 5$ considered in the present study. Finally, ΔB^* is again converted back to $\mathcal{R}$ values via the GQ model, now with the values of C_{f_0} corresponding to $Re_{\tau_0} = 1000$ and $Re_{\tau_0} = 2000$.

The comparison shows excellent agreement between the two datasets. This finding suggests very weak sensitivity of StTW actuation on the flow geometry (open channel versus closed plane channel) and further strengthens the reliability of the GQ16 data. In fact, due to their limited domain size, GQ16 had no data for $0 < \kappa^+ < 0.005$, but even there, the new data compare very well with the GQ16 map. The maximum difference between the present and GQ16 datasets evaluated across the interpolated maps shown in figure 4 is only 2.5 %, and the standard deviation is 0.8 %. The agreement shows that no measurable direct effect of large-scale turbulent structures on $\mathcal{R}$ exists at these values of Re_{τ_0} other than their possible contribution to C_{f_0}, which is already accounted for by the GQ model.

3.2. *Maps of ΔB^* : validity of the GQ model*

The GQ model relies on the hypothesis that, provided Re is high enough for the logarithmic law (1.3) to describe well the mean velocity profile, the quantity ΔB^* is a function of the control parameters only, and thus independent of the Reynolds number. This hypothesis is here tested using the ΔB^* maps for the DNS set at $Re_{\tau_0} = 1000$ and 2000. The maps are generated by applying the GQ model with the corresponding values of C_f, C_{f_0} and $\mathcal{R}$. The results, reported in figure 5, show maximum change of ΔB^* across Re of only 0.36, with standard deviation 0.10. These values can be considered quite small, given that the maximum statistical uncertainty on the change of ΔB^* at 95 % confidence level is 0.24 across the map of figure 5 and the mean absolute value is 0.17. This result thus confirms that the drag reduction effect barely changes with Re, once it is expressed in terms of ΔB^*.

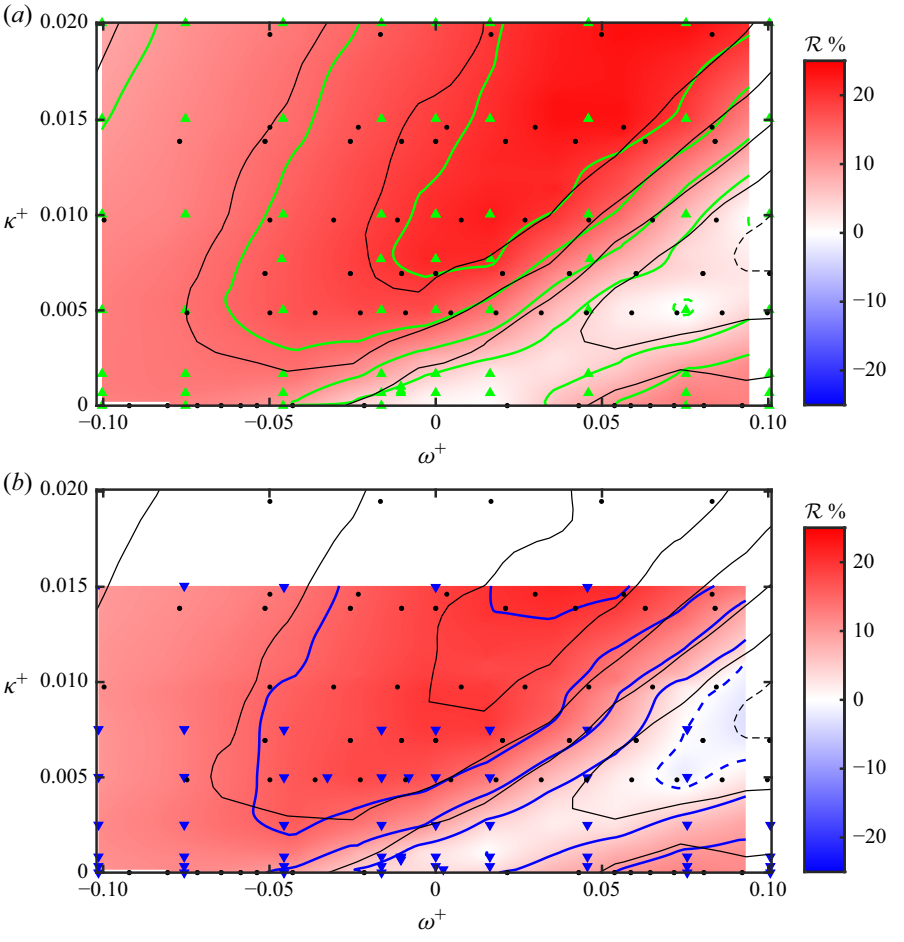

Figure 4. Maps of drag reduction ($\mathcal{R}$) as a function of actuation parameters (ω^+, κ^+), at (a) $Re_{\tau_0} = 1000$ and (*b*) $Re_{\tau_0} = 2000$. The colourmap, the contour lines and symbols coloured after table 1 refer to the present data, whereas the black contour lines and symbols refer to the data by GQ16, which at $Re_{\tau_0} = 2000$ are obtained from extrapolation through GQ model (1.4). The contour lines are every 5 % of $\mathcal{R}$, dashed lines mark the $\mathcal{R} = 0$ iso-line.

This additionally indicates that $Re_{\tau_0} = 1000$ is sufficient to obtain a reasonably Re-independent estimate of ΔB^*. This observation is also supported by the good agreement between the GQ16 data at $Re_{\tau_0} = 1000$ and the results by Rouhi *et al.* (2023) obtained up to $Re_{\tau_0} = 4000$ in relatively small domains.

3.3. *Monotonicity of $\mathcal{R}$ with Re*

The GQ model predicts that $\mathcal{R}$ decreases monotonically with Re; however, more slowly than the power-law decrease assumed in early studies (Choi, Xu & Sung 2002; Quadrio & Ricco 2004; Touber & Leschziner 2012). The decrease rate is less at higher Re and for smaller $\mathcal{R}$. Ample numerical and experimental evidence so far, including the results of the present study, support the predictions of the GQ model.

Contrasting evidence that $\mathcal{R}$ may instead increase with Re has been recently provided from the combined laboratory and numerical efforts of Marusic *et al.* (2021). As shown in figure 3(*e*) of their paper, they found that $\mathcal{R}$ obtained by backward-travelling waves at

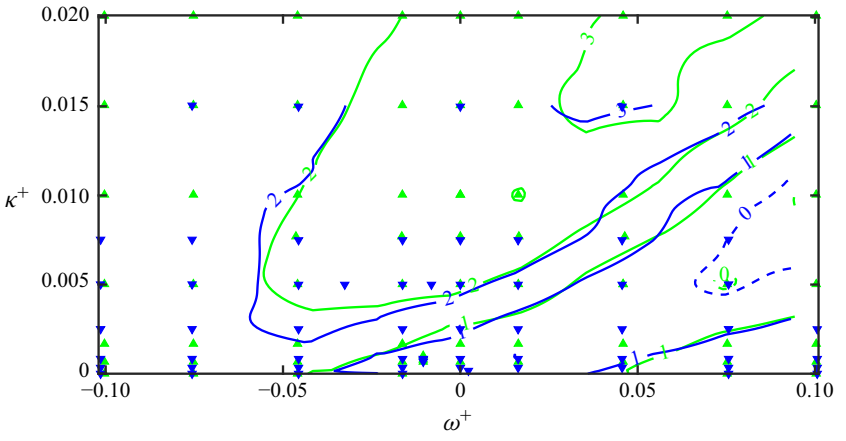

Figure 5. Maps of ΔB^* as a function of actuation parameters (ω^+, κ^+) at $Re_{\tau_0} = 1000$ (——) and $Re_{\tau_0} = 2000$ (——). The symbols are coloured after table 1 and show the parameters of each simulation underlying the map interpolation shown in the figure. Contours are shown in unit intervals, the dashed lines marking the $\Delta B^* = 0$ iso-line.

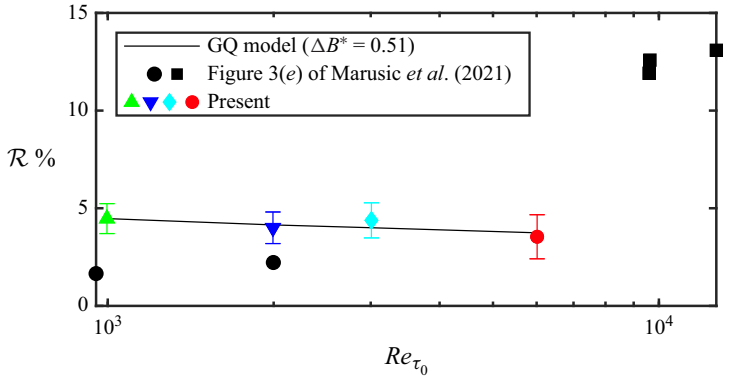

Figure 6. Drag reduction rate ($\mathcal{R}$) as a function of the reference friction Reynolds number (Re_{τ_0}) for backward-travelling wave with parameters $A^+ = 5$, $\kappa^+ = 0.00078$ and $\omega^+ = -0.0105$, close to the conditions considered by Marusic *et al.* (2021), i.e. $A^+ \approx 5$, $\kappa^+ \approx 0.0008$ and $\omega^+ \approx -0.0105$ (in their laboratory experiment, the viscous-scaled parameters vary slightly with Re). The present results are denoted with coloured symbols (see table 1); experimental data by Marusic *et al.* (2021) are black squares, while black circles denote their LES numerical data; the straight line is the prediction of the GQ model (1.4) corresponding to $\Delta B^* = 0.51$ and to the values of C_{f_0} obtained from the uncontrolled simulations at the respective value of Re_{τ_0}. The error bars have been determined as described in § 2, corresponding to a 95 % confidence level.

small values of κ^+ and ω^+, namely $\kappa^+ = 0.0008$ and $\omega^+ = -0.0105$, increases from 1.6 % at $Re_{\tau_0} \approx 1000$, as measured numerically in large eddy simulation (LES) of open channel flow, up to 13.1 % at $Re_{\tau_0} \approx 12\,800$, as measured experimentally in a turbulent boundary layer. Since the actuator employed in their experiments yields a wave with a frequency-dependent amplitude and constant wavelength in physical units (30 cm), those authors could not exactly maintain the same value of viscous-scaled control parameters across the considered Reynolds number range. Specifically, the amplitude increased from $A^+ = 4.6$ at $Re_\tau = 9000$ to $A^+ = 5.7$ at $Re_\tau = 12\,800$ (see table 1 of Chandran *et al.* (2023)). Furthermore, although the original figure 3(*e*) of Marusic *et al.* (2021) reports a constant

value of $\kappa^+ = 0.0008$ at all Re, we cannot reconcile it with the actuator wavelength being fixed in physical units for the experimental points.

In the present work, we verify this contrasting evidence by studying the Re dependence of $\mathcal{R}$ across the widest range of Reynolds number tested so far via DNS. For this purpose, we consider StTW actuation at $Re_{\tau_0} = 1000$, 2000, 3000 and 6000, with control parameters selected to match as closely as possible those reported in figure 3(*e*) of Marusic *et al.* (2021), namely $\kappa^+ = 0.00078$ and $\omega^+ = -0.0104$. The wave amplitude is set to $A^+ = 5$, midway between the range of variation in their experiments. Figure 6 compares our numerical results with the numerical and experimental results of Marusic *et al.* (2021). Our measurements still fit very well the prediction of the GQ model and confirm an overall decreasing trend of $\mathcal{R}$ with Re.

To verify whether the differences observed in figure 6 are due to the different Reynolds number range considered here and by Marusic *et al.* (2021), we advocate the work of Chandran *et al.* (2023). Those authors extended the experimental database of Marusic *et al.* (2021) with additional data points, some of which at $Re_{\tau_0} \approx 6000$, i.e. the highest Reynolds number considered in the present study. Hence, we have precisely reproduced their actuated flow case with $\{A^+, \omega^+, \kappa^+, Re_{\tau_0}\} = \{2.5, -0.009, 0.0014, 6000\}$, the remaining differences being the flow configuration (open channel versus boundary layer), as well as actuation details (ideal harmonic actuation in numerical simulation versus spatially discretised wave in experiment). This case also falls within the range of potential use for outer-scaled actuation according to Deshpande *et al.* (2023), due to the comparatively large actuation period $T^+ = -700$ and wavelength $\lambda^+ \approx 4500$, similar to the case presented in figure 6. A drag reduction of $\mathcal{R} = 2.3\,\% \pm 1.1\,\%$ is measured here, to be compared with $\mathcal{R} = 6\,\%$ measured experimentally by Chandran *et al.* (2023). This finding hints at systematic differences between the present numerical simulations and the laboratory experiments of Marusic *et al.* (2021) and Chandran *et al.* (2023). We reiterate that this is possibly due to irreducible differences in the flow and wall actuation set-ups, or even to the extreme challenges posed by laboratory experiments targeting such complex drag reduction strategies. We will go back to this important issue in § 4. For the moment, the present data corroborate the expectation that $\mathcal{R}$ decreases with Re at the rate predicted by the GQ model.

3.4. *Net power savings at large values of Re*

Net power saving $\mathcal{S}$ derives from the (positive or negative) balance between the power saved through drag-reducing control and the power required for wall actuation, hence,

$$\mathcal{S} = \mathcal{R} - \frac{P_{in}}{P_{p_0}}\,, \tag{3.1}$$

where P_{p_0} is the pumping power per unit wetted area in the uncontrolled case, which for constant U_b reads

$$P_{p_0} = U_b \tau_{x_0}\,, \tag{3.2}$$

and P_{in} is the control input power per unit wetted area, expressed as

$$P_{in} = \langle w_w \tau_z \rangle = \rho\nu \left\langle w \frac{\partial w}{\partial y} \right\rangle \bigg|_w = \frac{\rho\nu}{2} \frac{\mathrm{d}}{\mathrm{d}y} \langle w w \rangle \bigg|_w\,, \tag{3.3}$$

where $\tau_z = \rho\nu(\partial w/\partial y)_w$ is the spanwise wall shear stress.

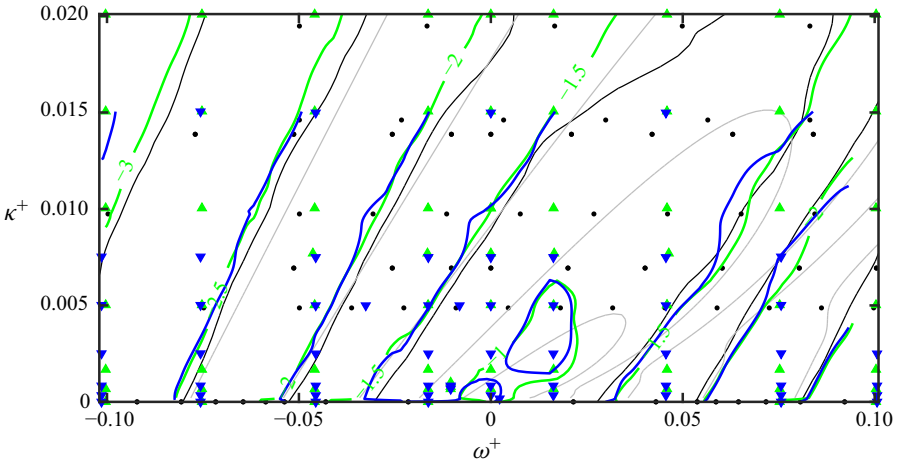

Figure 7. Maps of actuation power (P_{in}^+) as a function of the actuation parameters (ω^+, κ^+) at $Re_{\tau_0} = 1000$ (——) and $Re_{\tau_0} = 2000$ (——). The symbols are coloured after table 1 and show the parameters of each simulation underlying the map interpolation shown in the figure. Data by GQ16 (——) and P_{in}^+ from (3.4) (——) are also reported.

Similarly to what done for $\mathcal{R}$, the Reynolds number dependence of $\mathcal{S}$ can also be predicted theoretically. Whereas $\mathcal{R}$ is accurately expressed by the GQ model, the Re dependence of P_{in}/P_{p_0} can be easily expressed following Ricco & Quadrio (2008), who noticed that this ratio is equivalent to $P_{in}^+/P_{p_0}^+$. Since P_{in}^+ is very well approximated by the power P_ℓ^+ required to generate the laminar transverse Stokes layer (Quadrio & Ricco 2011; Gatti & Quadrio 2013) – which does not depend on Re if the viscous-scaled parameters are kept constant – the Re dependence of P_{in}/P_{p_0} comes only from $P_{p_0}^+ = U_b^+ = \sqrt{2/C_{f_0}}$. By using the expression of P_ℓ^+ by Gatti & Quadrio (2013), we thus obtain

$$\frac{P_{in}}{P_{p_0}} \approx \frac{P_\ell^+}{U_b^+} = \frac{(A^+)^2(\kappa^+)^{1/3}}{2U_b^+} Re\left[\mathrm{e}^{\pi i/6}\frac{Ai'(\theta)}{Ai(\theta)}\right], \tag{3.4}$$

where i is the imaginary unit, Re indicates the real part of a complex number, Ai is the Airy function of the first kind, Ai' its derivative and $\theta = -\mathrm{e}^{\pi i/6}(\kappa^+)^{1/3}(\omega^+/\kappa^+ + i\kappa^+)$. Equation (3.4) shows that $P_{in}^+ = U_b^+ P_{in}/P_{p_0} \approx P_\ell^+$ is a Reynolds-independent quantity for StTW parameters sufficiently far from the region of drag increase, where the approximation $P_{in}^+ \approx P_\ell^+$ is known to fail. As a result, it is sufficient to measure P_{in}^+ at a given Reynolds number, or estimate it via P_ℓ^+, to retrieve P_{in}/P_{p_0} at any Reynolds number, i.e. at any arbitrary $U_b^+ = \sqrt{2/C_{f_0}}$. Equation (3.4) shows that P_{in}/P_{p_0} decreases with Re as $1/U_b^+$, so that $\mathcal{S}$ can in fact increase with Re, provided the normalised actuation power decays with Re faster than $\mathcal{R}$.

Figure 7 confirms that P_{in}^+ is indeed constant with Re throughout the investigated parameter space, including the drag-increasing regime, where P_{in}^+ and P_ℓ^+ do differ and the former can only be measured empirically. The GQ16 dataset well aligns with the present data, the lacking information for $0 < \kappa^+ \leqslant 0.005$ notwithstanding.

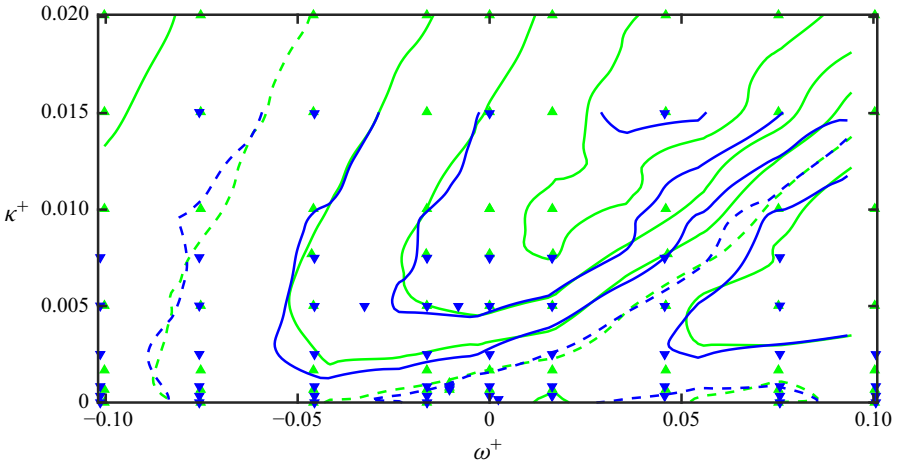

Figure 8. Maps of net power saving ($\mathcal{S}$) as a function of the actuation parameters (ω^+, κ^+) at $Re_{\tau_0} = 1000$ (——) and $Re_{\tau_0} = 2000$ (——). The symbols are coloured after table 1 and show the parameters of each simulation underlying the map interpolation shown in the figure. Contour lines are shown in intervals of 5 %, the dashed lines denoting the $\mathcal{S} = 0$ iso-line.

The net power saving at $Re_{\tau_0} = 1000$ and 2000 is reported in figure 8. Overall, the contours of $\mathcal{S}$ do not change significantly, since degradation of $\mathcal{R}$ is compensated by reduction of the actuation input power. Larger differences are observed for nearly optimal $\mathcal{S}$ (see the $\mathcal{S} = 15$ % iso-line in figure 8), in a region which shrinks and shifts towards higher κ^+ at higher Re. This can be explained by the stronger decay of $\mathcal{R}$ in this region (as predicted by the GQ model due to larger $\mathcal{R}$) and by the comparatively small value of P_{in}/P_{p_0}, which causes $\mathcal{S}$ to have similar Re dependence as $\mathcal{R}$.

GQ16 noticed that at $Re_{\tau_0} \approx 1000$ and $A^+ = 5.5$, the locus of near-optimum net power saving ($\mathcal{S} = 15$ %) extends along the ridge of maximum $\mathcal{R}$ between $\kappa^+ = 0.0085$ and 0.04, the maximum being at $\{\omega^+, \kappa^+\} = \{0.093, 0.026\}$. This implies that the point of maximum $\mathcal{S}$ might reside outside of the parameter space considered in figure 8 for both Reynolds numbers under scrutiny here.

As done for the drag reduction in figure 6, the variation of $\mathcal{S}$ with Re is shown in figure 9 for the same parameters considered by Marusic *et al.* (2021). Interestingly, $\mathcal{S}$ is observed to increase with Re at this combination of parameters, essentially due to the shrinking of the negative P_{in}/P_{p_0} contribution and to the relatively constant $\mathcal{R}$. The increase of $\mathcal{S}$ is compatible with the theoretical prediction that can be obtained by combining the GQ model of (1.4) with the prediction for P_{in}/P_{p_0} of (3.4). The differences between the present numerical database and the laboratory experiments of Marusic *et al.* (2021), previously noted for $\mathcal{R}$, are confirmed here.

The present results enable a better understanding of the available literature data. For instance, by comparing the numerical data by Rouhi *et al.* (2023), which consider StTW at small wavelengths (due to the restricted domain size) and relatively large amplitude $A^+ = 12$ and frequencies, with their experimental data, which consider backward-travelling waves at larger wavelengths but smaller amplitudes of $A^+ \approx 5$ and frequencies, Chandran *et al.* (2023) conclude that mostly low-frequency forcing $|\omega^+| < 0.018$ is capable to achieve positive $\mathcal{S}$, despite the moderate values of $\mathcal{R}$. This conclusion is observed here to be an artefact of the comparison between StTW at different amplitudes: according to GQ16, it is known that already at $Re_{\tau_0} = 1000$, no positive $\mathcal{S}$ can be achieved via StTW

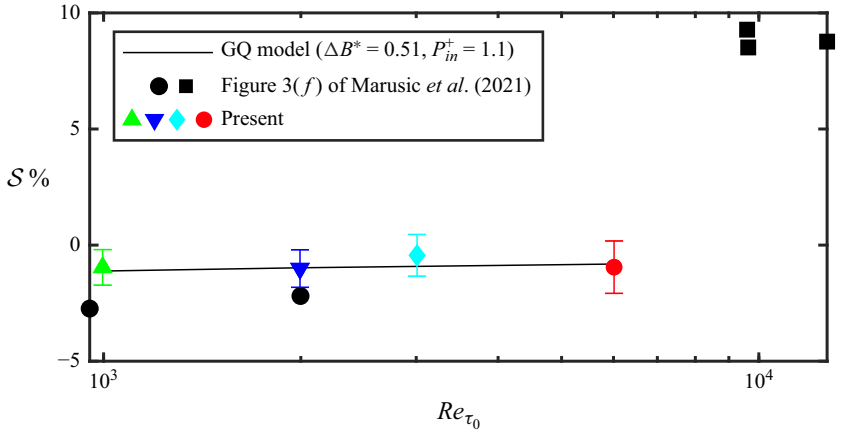

Figure 9. Net power saving ($\mathcal{S}$) as function of reference friction Reynolds number (Re_{τ_0}) for backward-travelling waves with the same parameters considered by Marusic *et al.* (2021). The present data are indicated with coloured symbols (see table 1); experimental data by Marusic *et al.* (2021) are black squares, while black circles denote their LES numerical data; the straight line is the theoretical prediction obtained by combining the GQ model (1.4) for $\Delta B^* = 0.51$ with (3.4) for $P_{in}^+ = 1.1$ and the values of C_{f_0} obtained from the uncontrolled simulations at the respective value of Re_{τ_0}.

for amplitudes $A^+ \gtrapprox 14$. The present data clearly show that the observation of GQ16 is valid also if smaller values of wavenumbers and frequencies are considered: the locus of maximum $\mathcal{S}$ in the $\{\omega, \kappa\}$-space essentially coincides with that of maximum $\mathcal{R}$, and it shifts towards larger $\{\omega, \kappa\}$ for increasing values of Re rather than to smaller ones if the comparison among various Re is performed at a constant value of A^+ close to the optimal $A^+ \approx 6$ identified by GQ16.

4. Concluding discussion

In the present work, we have addressed the Reynolds number dependence of skin-friction drag reduction induced by spanwise forcing, in terms of both drag reduction rate $\mathcal{R}$ and net power saving $\mathcal{S}$. In particular, we have focused on streamwise-travelling waves of spanwise wall velocity (StTW, Quadrio *et al.* 2009). A new database of high-fidelity direct numerical simulation (DNS) studies of turbulent open channel flow with and without StTW has been generated for $Re_{\tau_0} = 1000$, 2000, 3000 and 6000. This is the widest Reynolds number range considered so far in numerical experiments with spanwise forcing and reduces the gap from the highest value of Re_{τ_0} considered in analogous laboratory experiments (Chandran *et al.* 2023) to a factor of 2.5.

The main outcome of the present study is to confirm the validity of the predictive model for drag reduction proposed by Gatti & Quadrio (2016) and its underlying hypothesis. The present data corroborate the observation that the parameter ΔB^*, which quantifies the control-induced velocity shift in actual viscous units '$*$' at matched y^* with respect to the non-actuated flow is an Re-independent measure of drag reduction when the Reynolds number is sufficiently large for the logarithmic law to apply. We have shown that $Re_{\tau_0} \gtrapprox 1000$ is sufficient for ΔB^* to become nearly Re-independent, since no statistically significant differences have been measured between the $Re_{\tau_0} = 1000$ and $Re_{\tau_0} = 2000$ cases, for a wide range of actuation parameters, and up to $Re_{\tau_0} = 6000$ for one selected combination of actuation parameters.

This key result implies that drag reduction induced by StTW at a given combination of $\{A^+, \omega^+, \kappa^+\}$ is bound to monotonically decrease with the Reynolds number, at a rate that depends on $\mathcal{R}$ itself and on (the inverse square root of) the skin-friction coefficient C_{f_0} of the uncontrolled flow, as embodied in the GQ model; see (1.4). Fortunately, the decay rate is less severe than the power law $\mathcal{R} \sim Re_{\tau_0}^{-0.2}$ suggested empirically in early studies on spanwise wall oscillations (Choi *et al.* 2002; Touber & Leschziner 2012), conveying that significant drag reduction can still be achieved at very high Re.

The increase of drag reduction with the Reynolds number, observed by Marusic *et al.* (2021) with actuation parameters corresponding to the outer-scaled actuation, is not confirmed by our numerical experiments with $\{A^+, \omega^+, \kappa^+\} = \{5, -0.0104, 0.00078\}$ in turbulent open channels. In contrast, the present results follow well the prediction of the GQ model and show a very mild decrease of $\mathcal{R}$ with Re for these specific parameters. While the observation of $\mathcal{R}$ increasing with Re is indeed surprising and unique in the literature, we can only speculate on the reasons behind this discrepancy.

On the one hand, the difference in the flow set-up considered here and by Marusic *et al.* (2021) (open channel versus boundary layer) could affect the Reynolds number dependence of $\mathcal{R}$. In this respect, Skote (2014) applied StTW to numerical turbulent boundary layers at low Re and noted that the Kármán constant can increase in the presence of drag-reduction effects. This could affect the Re-dependency of $\mathcal{R}$, since the GQ model assumes constancy of k. However, this effect is only seen in the initial non-equilibrium state of the boundary layer, which was also corroborated by the experimental data of Chandran *et al.* (2023).

On the other hand, Marusic *et al.* (2021) and later Chandran *et al.* (2023) implemented a spatially discrete form of the StTW, similarly to Auteri *et al.* (2010), and synthesised harmonic waves by independently moving stripes with finite width. Auteri *et al.* (2010) and, more recently, Gallorini & Quadrio (2024) addressed the effects of the wave discretisation on the achievable drag reduction. Owing to discretisation, the turbulent flow perceives a number of higher Fourier harmonics of the discrete piecewise-constant wave, as if multiple waves with different parameters were applied. As a result, quantitative comparison between the ideally continuous and piecewise-constant forcing, as performed by Marusic *et al.* (2021) when comparing their numerical and experimental data, is not trivial, since some discrete waves far from the optimal forcing parameters can outperform the corresponding ideal sinusoidal waveform, whenever part of the harmonic content of the discrete wave falls in high-$\mathcal{R}$ regions of the drag reduction map.

We verify this hypothesis by reproducing the cases of figure 6 (StTW at $\{A^+, \omega^+, \kappa^+\} = \{5, -0.0104, 0.00078\}$) up to $Re_{\tau_0} = 3000$, this time employing discrete StTW instead of ideally continuous ones. Specifically, we discretise each wavelength into six pieceweise-constant streamwise stripes, similarly to the experiments by Marusic *et al.* (2021). Accordingly, the StTW boundary condition of (1.1) is replaced with its discrete counterpart, proposed by Gallorini & Quadrio (2024), as follows:

$$w(x, t; s) = A \sin\left(\omega t - \frac{2\pi i}{s}\right) \quad \text{for } \frac{i}{s}\lambda \leqslant x < \frac{i+1}{s}\lambda, \quad s = 6 \quad \text{and} \quad i \in \mathbb{N}. \tag{4.1}$$

With the results presented in figure 10, we cannot state that $\mathcal{R}$ increases with Re beyond statistical uncertainty also for discrete waves. However, as previously hypothesised and confirmed by Gallorini & Quadrio (2024), discrete waves with non-optimal parameters can outperform ideal continuous ones in terms of $\mathcal{R}$. In the present case, the considered discrete waves achieve approximately 1 % higher $\mathcal{R}$, albeit at the cost of a significantly increased input power: at $Re_{\tau_0} = 3000$, $\mathcal{S}$ is -0.95 for the continuous wave but -8.50 for the discrete one.

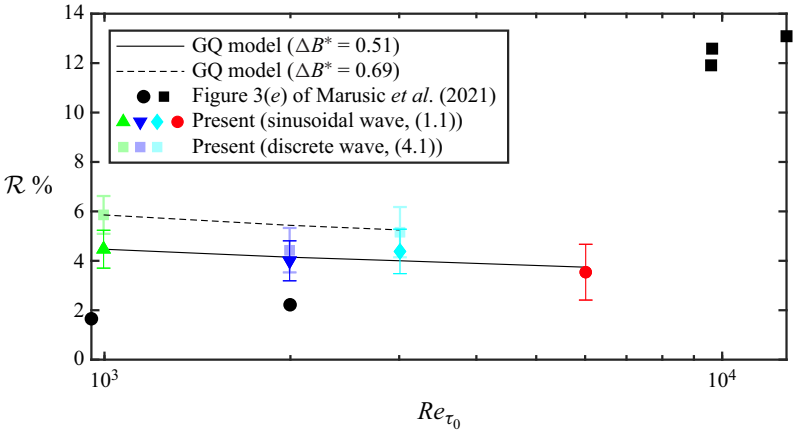

Figure 10. Drag reduction rate ($\mathcal{R}$) as a function of the reference friction Reynolds number (Re_{τ_0}) for backward-travelling wave with parameters $A^+ = 5$, $\kappa^+ = 0.00078$ and $\omega^+ = -0.0105$, close to the conditions considered by Marusic *et al.* (2021), i.e. $A^+ \approx 5$, $\kappa^+ \approx 0.0008$ and $\omega^+ \approx -0.0105$ (in their laboratory experiment the viscous-scaled parameters vary slightly with Re). This is a replica of figure 6 with the addition of the light coloured squares: these points have been obtained with discrete StTW, in which each wavelength has been discretised in six piecewise-constant streamwise sectors, and at the parameters mentioned previously.

The conclusion drawn by Marusic *et al.* (2021) that $\mathcal{R}$ increases with Re is based on data obtained with different methods. Specifically, the low-Re data were obtained from LES of turbulent open channel flow in relatively small domains with continuous StTW applied at the wall, whereas the high-Re data were obtained from boundary layer experiments with discrete StTW. As demonstrated previously, differences in flow configurations, methodologies and associated uncertainties complicate direct comparisons. Moreover, comparing discrete waves at high Re with ideal sinusoidal waves at low Re may introduce significant bias in interpreting the Re dependence of $\mathcal{R}$, particularly if discrete waves achieve greater $\mathcal{R}$. Additionally, estimating the ideal power consumption of discrete StTW using the expression valid for the ideal waves (e.g. (3.4)), as done by Marusic *et al.* (2021) and Chandran *et al.* (2023), significantly overestimates $\mathcal{S}$ and should be avoided.

Whereas the previous speculations remain to be verified in future studies, the present results support the claim that ideal StTW applied in turbulent open channels are neither expected nor observed to yield an increase of drag reduction with increasing Re for any combination of wave parameters that are kept constant in viscous units.

Lastly, we also confirm that the Reynolds number dependence of the net power saving $\mathcal{S} = \mathcal{R} - P_{in}/P_{p_0}$ is in line with theoretical predictions. Whereas $\mathcal{R}$ directly derives from the GQ model, P_{in}/P_{p_0} can be obtained directly from $P_{in}^+ = U_b^+ P_{in}/P_{p_0}$, which is known to be Re-independent (Gatti & Quadrio 2013). Interestingly, we have found that P_{in}^+ does not change with Re throughout the drag-reduction map, not only in those regions where P_{in}^+ is known to be well approximated by P_ℓ^+, i.e. the value obtained from the laminar generalised Stokes layer solution. In other words, the ideal viscous scaling of P_{in}^+ is retained even close to the valley of drag increase, where turbulence is known to interact with the generalised Stokes layer generated by StTW actuation. This result, as already discussed by Gatti & Quadrio (2013, 2016), has two main implications. First, in the portion of the StTW parameter space where $\mathcal{S}$ is maximum, $\mathcal{S}$ is dominated by $\mathcal{R}$ and hence exhibits similar Re dependence; here, $\mathcal{S}$ decreases with Re at a rate which is slightly less than $\mathcal{R}$. Second, for StTW parameters far from the optimum, both $\mathcal{R}$ and P_{in}/P_{p_0} contribute to $\mathcal{S}$. In this case, the normalised control cost may decrease with Re at

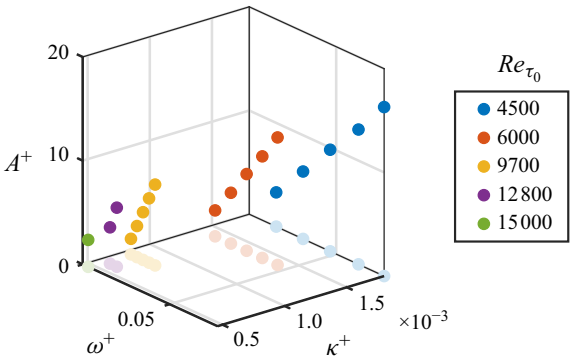

Figure 11. Wavenumber (κ^+), angular frequency (ω^+) and amplitude (A^+) for StTW actuation considered by Chandran *et al.* (2023) for different values of Re_{τ_0}. The lighter symbols show the projection of the data points onto the $\{\omega^+, \kappa^+\}$-plane.

a faster rate than $\mathcal{R}$, so that $\mathcal{S}$ can actually increase with Re. However, this can occur only in regions of non-optimal values of $\mathcal{S}$. Hence, we argue that the observation by Chandran *et al.* (2023) that only low-frequency, low-wavenumber forcing can achieve positive $\mathcal{S}$ at high Re may be an artefact due to the properties of their experimental set-up, in which the same region of the viscous-scaled parameter space cannot be spanned for different values of Re (see figure 11). Indeed, those authors can only achieve the optimal values of A^+ at the highest values of Re, at which only low ω^+ and κ^+ are possible owing to the small space and time scales of the turbulent flow. The more systematic scan of the StTW parameter space carried out in the present study shows that the loci of optimal $\mathcal{S}$ and $\mathcal{R}$ roughly coincide in the $\{\omega^+, \kappa^+\}$ plane.

Funding. This work was supported by the EuroHPC Joint Undertaking (JU) under grant EHPC-EXT-2022E01-054 on the Leonardo Booster machine at CINECA.

Declaration of interests. The authors report no conflict of interest.

Appendix A. Dataset details

This appendix reports the combination of the StTW control parameters of the simulations performed to produce the present dataset, together with the main quantities of interest. Tables 2, 3, 4 and 5 are for $Re_{\tau_0} = 1000$, $Re_{\tau_0} = 2000$, $Re_{\tau_0} = 3000$ and $Re_{\tau_0} = 6000$, respectively.

Case	A/U_b	A^+	$\omega h/U_b$	$\omega^+ \times 10^2$	κh	$\kappa^+ \times 10^2$	$\mathcal{R}$ %	$\mathcal{S}$ %
1	0.248	5.0	−4.98	−10.03	0	0.000	12.2	−1.6
2	0.248	5.0	−4.98	−10.03	0.67	0.067	12.7	−1.2
3	0.248	5.0	−4.98	−10.03	1.7	0.167	12.8	−1.3
4	0.248	5.0	−4.98	−10.03	5	0.502	12.6	−1.9
5	0.248	5.0	−4.98	−10.03	10	1.004	11.4	−3.6
6	0.248	5.0	−4.98	−10.03	15	1.506	9.8	−5.8
7	0.248	5.0	3.73	7.53	0	0.000	13.3	1.4
8	0.248	5.0	3.73	7.53	0.67	0.067	12.5	0.8
9	0.248	5.0	3.73	7.53	1.7	0.167	10.5	−1.0
10	0.248	5.0	4.98	10.03	0	0.000	12.2	−1.6
11	0.248	5.0	3.73	7.53	5	0.502	−1.0	−11.5
12	0.248	5.0	3.73	7.53	10	1.004	6.7	−2.0
13	0.248	5.0	3.73	7.53	15	1.506	19.3	12.9
14	0.248	5.0	4.98	10.03	0.67	0.067	12.0	−1.7
15	0.248	5.0	4.98	10.03	1.7	0.167	12.0	−1.5
16	0.248	5.0	4.98	10.03	5	0.502	5.4	−7.5
17	0.248	5.0	4.98	10.03	10	1.004	−1.8	−13.8
18	0.248	5.0	4.98	10.03	15	1.506	10.0	0.1
19	0.248	5.0	−2.30	−4.64	7.7	0.770	16.3	5.3
20	0.248	5.0	−0.82	−1.65	7.7	0.770	19.8	11.4
21	0.248	5.0	−0.00	−0.00	7.7	0.770	21.6	14.8
22	0.248	5.0	0.82	1.65	7.7	0.770	20.9	15.7
23	0.248	5.0	2.30	4.64	7.7	0.770	10.3	4.9
24	0.248	5.0	−2.28	−4.59	0	0.000	10.2	1.2
25	0.248	5.0	−0.81	−1.63	0	0.000	2.8	−3.1
26	0.248	5.0	−2.28	−4.59	0.67	0.067	11.8	2.5
27	0.248	5.0	−0.81	−1.63	0.67	0.067	5.3	−0.7
28	0.248	5.0	−0.00	−0.00	0.67	0.067	1.0	−3.4
29	0.248	5.0	0.81	1.63	0.67	0.067	0.8	−4.8
30	0.248	5.0	2.28	4.59	0.67	0.067	8.0	−0.8
31	0.248	5.0	−2.28	−4.59	1.7	0.167	14.3	4.8
32	0.248	5.0	−0.81	−1.63	1.7	0.167	10.3	3.9
33	0.248	5.0	−0.00	−0.00	1.7	0.167	4.7	−0.1
34	0.248	5.0	0.81	1.63	1.7	0.167	2.2	−2.1
35	0.248	5.0	2.28	4.59	1.7	0.167	3.5	−5.0
36	0.248	5.0	−2.28	−4.59	5	0.502	16.6	6.2
37	0.248	5.0	−0.81	−1.63	5	0.502	18.1	10.5
38	0.248	5.0	−0.00	−0.00	5	0.502	17.5	11.6
39	0.248	5.0	0.81	1.63	5	0.502	13.5	9.1
40	0.248	5.0	2.28	4.59	5	0.502	3.0	−3.8
41	0.248	5.0	2.28	4.59	5	0.502	3.0	−3.8
42	0.248	5.0	−2.28	−4.59	10	1.004	15.6	4.2
43	0.248	5.0	−0.81	−1.63	10	1.004	19.0	10.0
44	0.248	5.0	−0.00	−0.00	10	1.004	20.8	13.3
45	0.248	5.0	0.81	1.63	10	1.004	22.5	16.5
46	0.248	5.0	2.28	4.59	10	1.004	18.2	13.4
47	0.248	5.0	−2.28	−4.59	15	1.506	14.0	1.8
48	0.248	5.0	−0.81	−1.63	15	1.506	17.4	7.4
49	0.248	5.0	−0.00	−0.00	15	1.506	18.9	10.2
50	0.248	5.0	0.81	1.63	15	1.506	20.5	13.0
51	0.248	5.0	2.28	4.59	15	1.506	24.3	18.8
52	0.228	4.6	−0.00	−0.00	10	1.004	19.7	13.3
53	0.248	5.0	−0.52	−1.05	0.67	0.067	3.9	−1.0
54	0.248	5.0	−0.52	−1.05	1	0.100	5.4	−0.2
55	0.248	5.0	−3.73	−7.53	0	0.000	12.3	0.4

Table 2. For caption see next page

56	0.248	5.0	−3.73	−7.53	0.67	0.067	13.4	1.3
57	0.248	5.0	−3.73	−7.53	1.7	0.167	13.2	1.0
58	0.248	5.0	−3.73	−7.53	5	0.502	13.8	1.0
59	0.248	5.0	−3.73	−7.53	10	1.004	12.3	−1.2
60	0.248	5.0	−3.73	−7.53	15	1.506	11.8	−2.4
61	0.248	5.0	−4.98	−10.04	20	2.008	8.5	−7.7
62	0.248	5.0	−3.73	−7.53	20	2.008	10.8	−4.0
63	0.248	5.0	−2.28	−4.59	20	2.008	13.0	0.1
64	0.248	5.0	−0.81	−1.63	20	2.008	15.6	4.7
65	0.248	5.0	−0.00	−0.00	20	2.008	17.3	7.5
66	0.248	5.0	0.81	1.63	20	2.008	19.5	10.9
67	0.248	5.0	2.28	4.59	20	2.008	22.9	16.2
68	0.248	5.0	3.73	7.53	20	2.008	23.8	17.7
69	0.248	5.0	4.98	10.04	20	2.008	19.8	11.8
70	0.248	5.0	−0.52	−1.05	0.78	0.078	4.5	−1.0
71*	0.248	5.0	−0.52	−1.05	0.78	0.078	5.9	−6.9

Table 2 (cntd). List of the controlled simulations carried out at $Re_{\tau_0} = 1000$. In the last case, denoted with the superscript *, a discrete travelling wave has been imposed according to (4.1).

Case	A/U_b	A^+	$\omega h/U_b$	$\omega^+ \times 10^2$	κh	$\kappa^+ \times 10^2$	$\mathcal{R}\,\%$	$\mathcal{S}\,\%$
1	0.3	6.5	0.21	0.23	0.33	0.017	2.7	−2.1
2	0.228	5.0	−1.50	−1.63	0	0.000	1.9	−3.5
3	0.228	5.0	−4.19	−4.56	0	0.000	9.5	1.3
4	0.228	5.0	1.50	1.63	5	0.250	3.6	−0.4
5	0.228	5.0	−1.50	−1.63	0.67	0.033	5.2	−0.2
6	0.228	5.0	−4.19	−4.56	0.67	0.033	10.6	2.3
7	0.228	5.0	−0.00	−0.00	0.67	0.033	3.6	−0.1
8	0.228	5.0	4.19	4.56	0.67	0.033	9.0	0.8
9	0.228	5.0	1.50	1.63	0.67	0.033	3.2	−2.0
10	0.228	5.0	−1.50	−1.63	5	0.250	12.8	6.6
11	0.228	5.0	−4.19	−4.56	1.7	0.083	13.0	4.5
12	0.228	5.0	−0.00	−0.00	1.7	0.083	1.9	−2.2
13	0.228	5.0	4.19	4.56	1.7	0.083	8.3	0.3
14	0.228	5.0	1.50	1.63	1.7	0.083	−0.2	−5.2
15	0.228	5.0	−1.50	−1.63	10	0.500	18.2	11.3
16	0.228	5.0	−4.19	−4.56	5	0.250	16.0	7.1
17	0.228	5.0	−0.00	−0.00	5	0.250	9.5	4.9
18	0.228	5.0	4.19	4.56	5	0.250	0.7	−6.9
19	0.228	5.0	−1.50	−1.63	1.7	0.083	6.7	1.1
20	0.228	5.0	−4.19	−4.56	10	0.500	16.0	6.6
21	0.228	5.0	4.19	4.56	10	0.500	3.2	−3.1
22	0.228	5.0	−1.50	−1.63	15	0.749	18.0	10.4
23	0.228	5.0	−4.19	−4.56	15	0.749	15.9	5.9
24	0.228	5.0	−0.00	−0.00	15	0.749	19.7	13.5
25	0.228	5.0	4.19	4.56	15	0.749	11.5	6.5
26	0.228	5.0	1.50	1.63	15	0.749	19.3	14.6
27	0.228	5.0	−0.75	−0.81	10	0.500	17.4	11.2
28	0.228	5.0	−0.00	−0.00	30	1.499	18.5	10.5
29	0.228	5.0	−2.99	−3.26	10	0.500	17.3	8.9
30	0.228	5.0	1.50	1.63	10	0.500	12.8	8.7
31	0.228	5.0	−0.00	−0.00	10	0.500	16.5	11.2
32	0.228	5.0	−0.95	−1.05	1.7	0.084	4.3	−0.7

Table 3. For caption see next page.

33	0.228	5.0	−0.95	−1.05	1.3	0.067	3.1	−1.9
34	0.228	5.0	−4.19	−4.56	30	1.499	13.0	1.8
35	0.228	5.0	4.19	4.56	30	1.499	22.1	17.0
36	0.228	5.0	9.24	10.06	0	0.000	10.9	−1.9
37	0.228	5.0	9.24	10.06	0.67	0.033	11.4	−1.3
38	0.228	5.0	9.24	10.06	1.7	0.083	11.2	−1.4
39	0.228	5.0	9.24	10.06	5	0.250	10.0	−2.4
40	0.228	5.0	9.24	10.14	10	0.501	4.0	−7.9
41	0.228	5.0	9.24	10.14	15	0.752	−4.0	−15.2
42	0.228	5.0	−9.24	−10.14	0	0.000	10.7	−2.3
43	0.228	5.0	−9.24	−10.14	0.67	0.033	10.6	−2.1
44	0.228	5.0	−9.24	−10.14	1.7	0.084	11.1	−1.7
45	0.228	5.0	−9.24	−10.14	5	0.251	11.5	−1.5
46	0.228	5.0	−9.24	−10.14	10	0.501	10.5	−2.9
47	0.228	5.0	−9.24	−10.14	15	0.752	10.4	−3.2
48	0.228	5.0	−6.89	−7.56	0	0.000	11.9	1.0
49	0.228	5.0	−6.89	−7.56	0.67	0.033	11.6	0.6
50	0.228	5.0	−6.89	−7.56	1.7	0.084	12.0	1.0
51	0.228	5.0	−6.89	−7.56	5	0.251	13.1	1.7
52	0.228	5.0	−6.89	−7.56	10	0.501	12.4	0.7
53	0.228	5.0	−6.89	−7.56	15	0.752	12.5	0.5
54	0.228	5.0	6.89	7.56	0	0.000	12.5	1.6
55	0.228	5.0	6.89	7.56	0.67	0.033	11.3	0.5
56	0.228	5.0	6.89	7.56	1.7	0.084	10.9	0.1
57	0.228	5.0	6.89	7.56	5	0.251	7.0	−3.3
58	0.228	5.0	6.89	7.56	10	0.501	−2.1	−11.8
59	0.228	5.0	6.89	7.56	15	0.752	−0.2	−9.5
60	0.228	5.0	−6.89	−7.56	30	1.504	11.1	−1.9
61	0.228	5.0	−0.95	−1.05	1.6	0.078	4.0	−1.0
62*	0.228	5.0	−0.95	−1.05	1.6	0.078	4.4	−7.4

Table 3 (cntd). List of the controlled simulations carried out at $Re_{\tau_0} = 2000$. In the last case, denoted with the superscript *, a discrete travelling wave has been imposed according to (4.1).

Case	A/U_b	A^+	$\omega h/U_b$	$\omega^+ \times 10^2$	κh	$\kappa^+ \times 10^2$	$\mathcal{R}\,\%$	$\mathcal{S}\,\%$
1	0.219	5.0	−2.16	−1.65	0.67	0.022	3.1	−2.1
2	0.219	5.0	−0.00	−0.00	0.67	0.022	1.4	−2.1
3	0.219	5.0	2.16	1.65	0.67	0.022	1.3	−3.8
4	0.219	5.0	2.16	1.65	1.7	0.056	−0.5	−5.5
5	0.218	5.0	−1.37	−1.05	2.3	0.078	4.4	−0.4
6	0.218	5.0	−1.37	−1.05	2.7	0.089	4.7	−0.1
7*	0.218	5.0	−1.37	−1.05	2.3	0.078	5.2	−6.2

Table 4. List of the controlled simulations carried out at $Re_{\tau_0} = 3000$. In the last case denoted with the superscript * a discrete travelling waves has been imposed according to (4.1).

Case	A/U_b	A^+	$\omega h/U_b$	$\omega^+ \times 10^2$	κh	$\kappa^+ \times 10^2$	$\mathcal{R}\,\%$	$\mathcal{S}\,\%$
1	0.203	5.0	−2.55	−1.04	4.7	0.078	3.5	−0.9
2	0.101	2.5	−2.19	−0.90	8.3	0.139	2.3	1.2

Table 5. List of the controlled simulations carried out at $Re_{\tau_0} = 6000$.

References

Auteri, F., Baron, A., Belan, M., Campanardi, G. & Quadrio, M. 2010 Experimental assessment of drag reduction by traveling waves in a turbulent pipe flow. *Phys. Fluids* **22** (11), 115103–115114.

Banchetti, J., Luchini, P. & Quadrio, M. 2020 Turbulent drag reduction over curved walls. *J. Fluid Mech.* **896**, 1–23.

Bernardini, M. & Pirozzoli, S. 2011 Inner/outer layer interactions in turbulent boundary layers: a refined measure for the large-scale amplitude modulation mechanism. *Phys. Fluids* **23** (6), 061701.

Bird, J., Santer, M. & Morrison, J.F. 2018 Experimental control of turbulent boundary layers with in-plane travelling waves. *Flow Turbul. Combust.* **100** (4), 1015–1035.

Chandran, D., Zampiron, A., Rouhi, A., Fu, M.K., Wine, D., Holloway, B., Smits, A.J. & Marusic, I. 2023 Turbulent drag reduction by spanwise wall forcing. Part 2: High-Reynolds-number experiments. *J. Fluid Mech.* **968**, A7.

Choi, J.-I., Xu, C.-X. & Sung, H.J. 2002 Drag reduction by spanwise wall oscillation in wall-bounded turbulent flows. *AIAA J.* **40** (5), 842–850.

Clauser, F.H. 1954 Turbulent boundary layers in adverse pressure gradients. *J. Aeronaut. Sci.* **21** (2), 91–108.

Deshpande, R., Chandran, D., Smits, A.J. & Marusic, I. 2023 On the relationship between manipulated inter-scale phase and energy-efficient turbulent drag reduction. *J. Fluid Mech.* **972**, A12.

Deshpande, R., Kidanemariam, A.G. & Marusic, I. 2024 Pressure drag reduction via imposition of spanwise wall oscillations on a rough wall. *J. Fluid Mech.* **979**, A21.

Dogan, E., Örlü, R., Gatti, D., Vinuesa, R. & Schlatter, P. 2019 Quantification of amplitude modulation in wall-bounded turbulence. *Fluid Dyn. Res.* **51** (1), 011408.

Flores, O. & Jiménez, J. 2010 Hierarchy of minimal flow units in the logarithmic layer. *Phys. Fluids* **22** (7), 071704.

Gallorini, E. & Quadrio, M. 2024 Spatial discretization effects in spanwise forcing for turbulent drag reduction. *J. Fluid Mech.* **982**, A11.

Garcia-Mayoral, R. & Jiménez, J. 2011 Hydrodynamic stability and the breakdown of the viscous regime over riblets. *J. Fluid Mech.* **678**, 317–347.

Gattere, F., Zanolini, M., Gatti, D., Bernardini, M. & Quadrio, M. 2024 Turbulent drag reduction with streamwise-travelling waves in the compressible regime. *J. Fluid Mech.* **987**, A30.

Gatti, D. & Quadrio, M. 2013 Performance losses of drag-reducing spanwise forcing at moderate values of the Reynolds number. *Phys. Fluids* **25** (12), 125109–125117.

Gatti, D. & Quadrio, M. 2016 Reynolds-number dependence of turbulent skin-friction drag reduction induced by spanwise forcing. *J. Fluid Mech.* **802**, 553–558.

Gatti, D., Stroh, A., Frohnapfel, B. & Hasegawa, Y. 2018 Predicting turbulent spectra in drag-reduced flows. *Flow Turbul. Combust.* **100** (4), 1081–1099.

Hama, F.R. 1954 Boundary-layer characteristics for rough and smooth surfaces. *Soc. Nav. Archit. Mar. Engrs* **62**, 333–351.

Hurst, E., Yang, Q. & Chung, Y.M. 2014 The effect of Reynolds number on turbulent drag reduction by streamwise travelling waves. *J. Fluid Mech.* **759**, 28–55.

Jiménez, J. 2004 Turbulent flows over rough walls. *Annu. Rev. Fluid Mech.* **36** (1), 173–196.

Jiménez, J. 2018 Coherent structures in wall-bounded turbulence. *J. Fluid Mech.* **842** (P1), 1–99.

Jiménez, J. & Moin, P. 1991 The minimal flow unit in near-wall turbulence. *J. Fluid Mech.* **225**, 213–240.

Jung, W.J., Mangiavacchi, N. & Akhavan, R. 1992 Suppression of turbulence in wall-bounded flows by high-frequency spanwise oscillations. *Phys. Fluids A* **4** (8), 1605–1607.

Kasagi, N., Hasegawa, Y. & Fukagata, K. 2009 Towards cost-effective control of wall turbulence for skin-friction drag reduction. In *Advances in Turbulence XII*, (ed. B.Eckhardt), vol. 132, pp. 189–200. Springer.

Kim, J. & Moin, P. 1985 Application of a fractional-step method to incompressible Navier–Stokes equations. *J. Comput. Phys.* **59** (2), 308–323.

Leonardi, S., Orlandi, P., Djenidi, L. & Antonia, R.A. 2015 Heat transfer in a turbulent channel flow with square bars or circular rods on one wall. *J. Fluid Mech.* **776**, 512–530.

Liu, X., Zhu, H., Bao, Y., Zhou, D. & Han, Z. 2022 Turbulence suppression by streamwise-varying wall rotation in pipe flow. *J. Fluid Mech.* **951**, A35.

Luchini, P. 1996 Reducing the turbulent skin friction. In *Computational Methods in Applied Sciences* (ed. J.A Désidéri, C. Hirsch, P. Le Tallec, E. Oñate, M. Pandolfi, J Périaux & E. Stein). Wiley.

Marusic, I., Chandran, D., Rouhi, A., Fu, M.K., Wine, D., Holloway, B., Chung, D. & Smits, A.J. 2021 An energy-efficient pathway to turbulent drag reduction. *Nat. Commun.* **12** (1), 5805.

Nikuradse, J. 1933 Strömungsgesteze in Rauhen Rohren. *VDI Forsch.* **361**.

Orlandi, P. 2006 *Fluid Flow Phenomena: A Numerical Toolkit*. Kluwer Academic Publishers.

PIROZZOLI, S. 2023 Searching for the log law in open channel flow. *J. Fluid Mech.* **971**, A15.
PIROZZOLI, S. & ORLANDI, P. 2021 Natural grid stretching for DNS of wall-bounded flows. *J. Comput. Phys.* **439**, 110408.
QUADRIO, M. 2011 Drag reduction in turbulent boundary layers by in-plane wall motion. *Phil. Trans. R. Soc. A* **369** (1940), 1428–1442.
QUADRIO, M., CHIARINI, A., BANCHETTI, J., GATTI, D., MEMMOLO, A. & PIROZZOLI, S. 2022 Drag reduction on a transonic airfoil. *J. Fluid. Mech.* **942**, 1–10.
QUADRIO, M., FROHNAPFEL, B. & HASEGAWA, Y. 2016 Does the choice of the forcing term affect flow statistics in DNS of turbulent channel flow? *Eur. J. Mech. - B/Fluids* **55**, 286–293.
QUADRIO, M. & RICCO, P. 2004 Critical assessment of turbulent drag reduction through spanwise wall oscillations. *J. Fluid Mech.* **521**, 251–271.
QUADRIO, M. & RICCO, P. 2011 The laminar generalized Stokes layer and turbulent drag reduction. *J. Fluid Mech.* **667**, 135–157.
QUADRIO, M., RICCO, P. & VIOTTI, C. 2009 Streamwise-traveling waves of spanwise wall velocity for turbulent drag reduction. *J. Fluid Mech.* **627**, 161–178.
RICCO, P., OTTONELLI, C., HASEGAWA, Y. & QUADRIO, M. 2012 Changes in turbulent dissipation in a channel flow with oscillating walls. *J. Fluid Mech.* **700**, 77–104.
RICCO, P. & QUADRIO, M. 2008 Wall-oscillation conditions for drag reduction in turbulent channel flow. *Intl J. Heat Fluid Flow* **29** (4), 601–612.
RICCO, P., SKOTE, M. & LESCHZINER, M.A. 2021 A review of turbulent skin-friction drag reduction by near-wall transverse forcing. *Prog. Aerosp. Sci.* **123**, 100713.
ROUHI, A., FU, M.K., CHANDRAN, D., ZAMPIRON, A., SMITS, A.J. & MARUSIC, I. 2023 Turbulent drag reduction by spanwise wall forcing. Part 1: Large-Eddy simulations. *J . Fluid Mech.* **268**, A6.
RUSSO, S. & LUCHINI, P. 2017 A fast algorithm for the estimation of statistical error in DNS (or experimental) time averages. *J. Comput. Phys.* **347**, 328–340.
SKOTE, M. 2014 Scaling of the velocity profile in strongly drag reduced turbulent flows over an oscillating wall. *Intl J. Heat Fluid Flow* **50**, 352–358.
SKOTE, M. 2022 Drag reduction of turbulent boundary layers by travelling and non-travelling waves of spanwise wall oscillations. *Fluids* **7** (2), 65.
SKOTE, M., SCHLATTER, P. & WU, Y. 2015 Numerical studies of active control of turbulent boundary layers using transverse travelling waves. In International Symposium On Turbulence and Shear Flow Phenomena (TSFP-9), pp. 6. University of Melbourne.
SPALART, P.R. & MCLEAN, J.D. 2011 Drag reduction: enticing turbulence, and then an industry. *Phil. Trans. R. Soc. A* **369** (1940), 1556–1569.
TOUBER, E. & LESCHZINER, M.A. 2012 Near-wall streak modification by spanwise oscillatory wall motion and drag-reduction mechanisms. *J. Fluid Mech.* **693**, 150–200.
VIOTTI, C., QUADRIO, M. & LUCHINI, P. 2009 Streamwise oscillation of spanwise velocity at the wall of a channel for turbulent drag reduction. *Phys. Fluids* **21** (11), 115109.
YAO, J., CHEN, X. & HUSSAIN, F. 2022 Direct numerical simulation of turbulent open channel flows at moderately high Reynolds numbers. *J. Fluid Mech.* **953**, A19.